

# Unlocking distributed acoustic sensing amplitude information through coherency coupling quantification

Thomas S. Hudson  \* 1,2, Anna Stork , Jack Muir , Andreas Fichtner 

<sup>1</sup>Department of Earth and Planetary Sciences, ETH Zurich, Zurich, Switzerland, <sup>2</sup>Department of Earth Sciences, University of Oxford, Oxford, UK, <sup>3</sup>Silixa Ltd, Elstree, UK, <sup>4</sup>Fleet Space Technologies, Adelaide, Australia

Author contributions: *Methodology*: T. Hudson. *Formal Analysis*: T. Hudson, A. Stork, J. Muir. *Writing - original draft*: T. Hudson.

**Abstract** Distributed Acoustic Sensing (DAS) allows one to measure strain at metre-resolution along a fibreoptic cable, increasing the density of spatial sampling of a seismic wavefield compared to conventional instrumentation. However, the challenge of measuring DAS-derived strain amplitude currently limits applications of this technology. Amplitude measurements are required in passive seismology for estimating earthquake magnitudes, moment tensor inversion and attenuation tomography, for example. For active seismic studies, amplitude information is essential for methods such as Amplitude Versus Offset (AVO) analysis. Central to this challenge is quantifying how well the fibre is coupled to the subsurface. Here, we present a method using coherency to pragmatically estimate coupling of fibre to the medium. We first introduce a theoretical justification relating coherency to relative coupling between channels and calibrating this to obtain absolute coupling coefficients, before evidencing the performance of the method using various examples from glaciers to downhole geothermal deployments. We apply the method to estimate earthquake magnitudes, comparing values to independent geophone estimates. The results allow us to explore whether quantifying coupling is possible or indeed necessary to account for in certain instances. We find that although coupling of fibre to the medium is important, results suggest that practically in many cases, it may be appropriate to simply make the binary first-order assumption that fibre is either approximately perfectly coupled or too poorly coupled for any amplitude analysis. While our findings do not comprehensively solve the fibre-optic coupling problem, the theory and results provide a practical foundation with which to start using DAS-derived amplitude information in earnest.

**Non-technical summary** Distributed Acoustic Sensing (DAS) is a nascent technology, converting fibreoptic cables into strain sensors that provide far denser spatial sampling than traditional seismometers. However, unlocking absolute amplitude measurements using DAS is currently challenging, limiting seismology applications. Measuring the amplitude is essential for estimating the size of earthquakes and imaging seismic energy loss in the subsurface, for example. Central to the DAS amplitude challenge is estimating how well coupled the fibre is to the subsurface. Here, we describe a new method that uses the similarity of the wavefield along a fibreoptic cable to estimate how well a fibreoptic cable is coupled to the subsurface. We first justify the method using theory, before showing how the method performs in a variety of contexts. The results not only show how coupling can be estimated, but allow us to explore whether one needs to even worry about coupling at all in certain instances. Our method provides a way of identifying and removing such channels from subsequent analysis. While our findings do not completely solve the fibreoptic coupling problem, it provides a practical foundation to start unlocking amplitude measurements from fibreoptic strain data.

## 1 Introduction

Amplitude measurements are important for estimating earthquake magnitudes, moment tensor inversion and attenuation tomography, for example. Distributed Acoustic Sensing (DAS) is a nascent technology that allows one to measure strain(-rate) at metre-resolution along a fibreoptic cable, increasing both spatial and temporal sampling of a seismic wavefield, compared to traditional instrumentation (Lindsey and Martin, 2021).

However, although DAS shows promise for interrogating a variety of seismic signals (for example, Hudson et al., 2021; Jousset et al., 2022; Klaasen et al., 2021; Lel-

louch et al., 2021; Spica et al., 2022; Walter et al., 2014; Williams et al., 2022; Zhan, 2019), unlocking absolute amplitude information remains challenging. Central to this challenge is quantifying coupling of fibreoptic cables to the surrounding medium. Although methods of obtaining DAS amplitude-frequency response and converting between strain(-rate) and displacement exist (Lindsey et al., 2020; Paitz et al., 2020; Trabattoni et al., 2023), which enable earthquake magnitudes to be estimated (Chen, 2023; Lellouch et al., 2020, 2021; Lior et al., 2023; Yin et al., 2023), coupling effects are not explicitly accounted for. Promising advances have recently been made in theoretical descriptions of the fibreoptic coupling problem (Reinsch et al., 2017), nu-

Production Editor:  
Yen Joe Tan  
Handling Editor:  
Wenbo Wu  
Copy & Layout Editor:  
Tara Nye

Signed reviewer(s):  
Yann Capdeville

Received:  
October 14, 2024  
Accepted:  
January 27, 2025  
Published:  
March 10, 2025

\*Corresponding author: thomas.hudson@eaps.ethz.ch

merically simulating fibreoptic coupling response (Celli et al., 2023), and ways to maximise coupling (Harmon et al., 2022), yet a means of quantifying coupling in-the-field does not yet exist. Furthermore, accurate quantification of fibreoptic coupling is hypothesised to be a critical limiting factor in amplitude-based DAS analysis, yet studies using conventional instrumentation regularly assume perfect coupling to the medium. This raises the legitimate question of whether the same assumption is valid for DAS in certain instances.

Here, we address the questions: (1) can fibre-medium coupling at least approximately be quantified? and (2) is it ever valid to assume perfect coupling of fibreoptic cables to the medium? We first provide a theoretical basis for quantifying relative coupling along fibreoptic cables using a simple coherency-based measurement, along with justifications of how to pragmatically convert these to absolute coupling coefficients. We then demonstrate the effectiveness of the method on real data, and explore whether coupling issues are always a fundamental limitation for measuring DAS-derived strain amplitude measurements. Specifically, we compare using the ambient noise wavefield to regional or teleseismic earthquake wavefields to quantify coupling. We then explore the importance of compensating for fibre-medium coupling issues using earthquake moment magnitudes for two diverse experiments, a glacier and a geothermal borehole. We emphasise from the outset that we endeavour here to provide a pragmatic solution to approximately quantify coupling, adequate for measuring DAS-derived absolute strain(-rate) amplitudes. This work should therefore be viewed as a step towards fully reconciling such measurements rather than fully resolving the challenging fibreoptic amplitude measurement problem.

## 2 Methods

### 2.1 Theoretical basis for coherency-based coupling coefficients

Although real-world fibre-medium coupling is complex, some simple assumptions allow one to formulate an analytical approximation that includes the essential physics. Our aim here is not to attempt to describe the complete coupling behaviour, but instead prove that at least to first order, one can approximately quantify relative coupling by comparing the coherency of neighbouring channels.

Figure 1 shows a schematic representation of our analytical fibre coupling model. This model describes the transfer of energy from the medium to the fibre (i.e. coupling) from an elastic perspective. We also include viscoelastic components to describe the concept of energy loss. This model is inspired by the work of Reinsch et al. (2017), Hubbard et al. (2022) and Celli et al. (2023). We point readers to these works if they wish to explore the theoretical basis for our model beyond that described here. In reality, it is impossible to isolate coupling variation over scales less than the DAS channel spacing. Over such spatial scales, our coupling model therefore combines coupling with any local het-

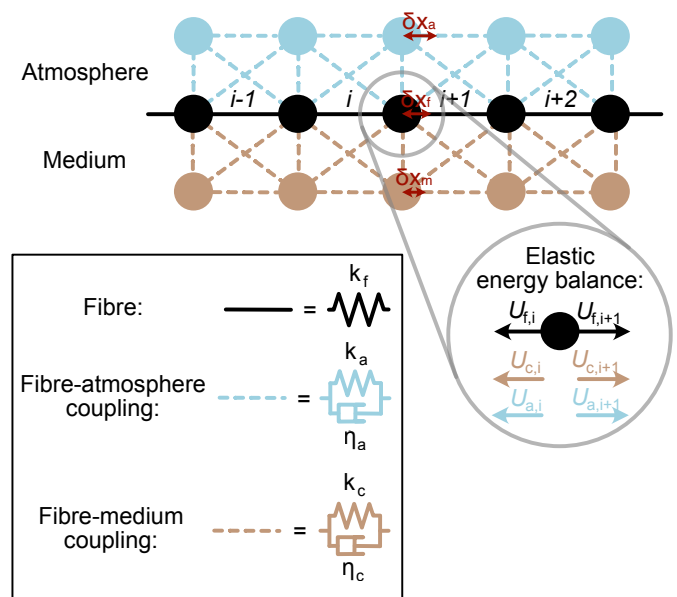


**Figure 1** Theoretical basis for fibreoptic coupling. The schematic is partially inspired by Celli et al. (2023). Attenuation is included via a Kelvin-Voigt visco-elastic model.

erogeneities.

For our model, let us assume that a section of fibre can be described by a set of springs in series, separated by nodes representing measurement points along the fibre. These nodes are also connected by spring-damper systems to both the medium and the atmosphere (see Figure 1). The spring-damper systems represent the coupling of each section of fibre to the medium and atmosphere, respectively. The fibre coupling to the medium and atmosphere at each node is controlled by the spring stiffness, with stiffness tending to zero describing coupling tending to zero. Damping represents attenuation, or energy loss, in the coupling mechanism. This system represents a fibre deployed horizontally at or near the surface, but one could simply translate this system for fibre buried sufficiently deep or for subsurface applications (for example, a borehole) by removing the atmospheric coupling components.

The coupling mechanism description in Figure 1 is valid for static friction cases, where the force between the medium and the fibre is less than the friction coefficient multiplied by the normal force. At one extreme, the fibre could be perfectly bonded to the medium (for example, tight fibre cemented into a borehole), for which this description holds. At the other extreme, dynamic friction could start to play a role, which would require a reformulation of the problem. The static friction regime should apply in the majority of current DAS use cases.

Let us then consider one fibre node, adjacent to two coincident sections of the fibre. We define these nodes as points between fibre channels, with strain measured at one channel representing the displacement between two nodes. The displacement of every node is somewhat coupled to every other node in the fibre. However, for simplicity let us assume here that this behaviour simply acts as a static pre-stress, with dynamic coupling

of an individual channel to neighbouring channels only. One can step up the complexity and assume interaction of more sections, and we discuss this in more detail later, when addressing gauge length effects. Let us also assume that the incident seismic wavefield is comprised of wavelengths  $\lambda > 2x_{ch}$ , where  $x_{ch}$  is the channel-spacing between nodes. This assumption is not necessary, but makes the theoretical relationship between coherency and coupling simpler to communicate. For now, let us also neglect the damping terms. The in-axis fibre energy balance can then be written as,

$$\begin{aligned} k_{m,i}\delta x_{m,i}^2 + k_f\delta x_{f,i}^2 + k_{a,i}\delta x_{a,i}^2 \\ = k_{m,i+1}\delta x_{m,i+1}^2 + k_f\delta x_{f,i+1}^2 + k_{a,i+1}\delta x_{a,i+1}^2, \end{aligned} \quad (1)$$

where  $k_{\gamma,i}$  is the spring stiffness for the coupling to the medium ( $m$ ), the fibre ( $f$ ) and the atmosphere ( $a$ ), respectively, at the location  $i$  along the fibre. Similarly,  $\delta x_{\gamma,i}$  is the change in displacement at location  $i$  along the fibre for the medium, fibre and atmosphere (see Figure 1). For simplicity, let us start by assuming that the fibre is perfectly isolated from the atmosphere, with  $k_{a,i}, k_{a,i+1} \approx 0$ . If  $\lambda > 2x_{ch}$ , the change in length of the medium between both sections of fibre can be approximated as equal after accounting for any moveout, so  $\delta x_{m,i+1} = \delta x_{m,i}$ . This assumes that any medium heterogeneities and coupling can be combined by variations in  $k_m$ . This can be rearranged to find the relative differences in length changes between the two fibre sections,

$$\begin{aligned} \Delta x_{f,i,i+1} &= \delta x_{f,i} - \delta x_{f,i+1} \\ &= \frac{k_{m,i+1}\delta x_{m,i+1}^2 - k_{m,i}\delta x_{m,i}^2}{k_f(\delta x_{f,i} + \delta x_{f,i+1})}. \end{aligned} \quad (2)$$

This is the basis of coherency between channels, with two channels perfectly coherent in strain,  $\varepsilon$ , if  $\delta x_{f,i} = \delta x_{f,i+1}$  ( $\Delta x_{f,i,i+1} = 0$ ). The effect of coupling is therefore controlled by  $k_{m,i}$  and  $k_{m,i+1}$ .

A simple thought experiment to demonstrate the relationship between coherency and coupling is to assume two channels are both perfectly coupled to the medium ( $k_{m,i}, k_{m,i+1} = 1$ ) and  $\lambda > 2x_{ch}$  so that  $\delta x_{m,i} = \delta x_{m,i+1}$ . In this case,  $\Delta x_{f,i,i+1}$  is zero and hence the strain along sections  $i$  and  $i + 1$  are perfectly equal and coherent. Conversely, the same thought experiment can also be applied for the case of two perfectly uncoupled channels, where again the two channels would be perfectly equal and coherent. Coherency therefore provides a measure of relative coupling rather than absolute coupling between channels. However, in the perfectly uncoupled scenario, no signals from the medium would be transmitted to the fibre. We therefore expect it to be straight-forward to discriminate perfectly uncoupled from perfectly coupled channels in practice.

How one measures coherency dictates how one quantifies the fibre-medium coupling of each node, or channel,  $k_{m,i}$ . Here, we opt for measuring the coherency between adjacent channels using the scalar product between two channels in the time-domain (equivalent to zero-lag cross-correlation in the time-domain; Prieto et al., 2009b), although we also investigate frequency-domain measurements. Using the scalar product to derive coherency is related to the fractional difference,  $A_i$ ,

in strain between two sections,  $\varepsilon_i$  and  $\varepsilon_{i+1}$ . Explicitly, strain at channel  $i$  is given by,

$$\varepsilon_i(t) = \frac{\delta x_{f,i}(t)}{x_{ch}}. \quad (3)$$

Since  $x_{ch}$  is constant,  $A_i$  can then be defined by rearranging Eq. 2,

$$\begin{aligned} A_i &= \frac{\delta x_{f,i}}{\delta x_{f,i+1}} \\ &= 1 + \frac{k_{m,i+1}\delta x_{m,i+1}^2 - k_{m,i}\delta x_{m,i}^2}{k_f(\delta x_{f,i} + \delta x_{f,i+1})\delta x_{f,i+1}}. \end{aligned} \quad (4)$$

The ratio of displacement (and hence strain) between fibre channels,  $A_i$ , can be measured by taking the scalar product of the strain time-series measured across adjacent sections  $i$  and  $i + 1$  (effectively a zero-lag cross-correlation). The normalised scalar product providing a measure of coherency in the time-domain,  $C_i$ , is given by,

$$\begin{aligned} C_i &= \sum_{t=0}^{t=t_{win}} \frac{\varepsilon_i(t) \cdot \varepsilon_{i+1}(t)}{|\varepsilon_i(t)| \cdot |\varepsilon_{i+1}(t)|} \\ &= \sum_{t=0}^{t=t_{win}} \frac{A_i \varepsilon_i(t)^2}{|A_i| |\varepsilon_i(t)|^2} \\ &= \sum_{t=0}^{t=t_{win}} \frac{A_i}{|A_i|}, \end{aligned} \quad (5)$$

where  $t_{win}$  is the duration of the time-window over which the cross-correlation is performed. The scalar product coherency,  $C_i$ , is therefore proportional to the normalised value of  $A_i$ .

However, if there is any moveout between waves arriving at consecutive channels, then  $\varepsilon_i(t) \neq A_i \varepsilon_{i+1}(t)$ . In this instance, Eq. 5 can be modified such that  $\varepsilon_i(t) = A_i \varepsilon_{i+1}(t + \tau)$ , where  $\tau$  is a non-zero lag accounting for the moveout. From hereon in, any lags are accounted for by shifting any data in time to maximise the value of the scalar product coherency,  $C_i$ .

A similar alternative formulation to quantify coherence in the frequency domain would be an adaptive covariance filter (Du et al., 2000; Nakata et al., 2015; Samson and Olson, 1981). In the instance where the fibre is perfectly isolated from the atmosphere ( $k_{a,i}, k_{a,i+1} = 0$ ),  $A_i$  and therefore  $C_i$  both vary between 0 and 1, varying only with the relative coupling between channels,  $|k_{m,i+1} - k_{m,i}|$ . Therefore,  $C_i$  represents the relative coupling coefficient of the fibre in this regime.

## 2.2 A note on relative vs. absolute coupling coefficients

Relative coupling is already useful. Values can be used to discriminate poorly-coupled channels from well-coupled channels and weighted accordingly. Or, for moment tensor inversion (Hudson et al., 2021), only relative amplitudes and therefore relative coupling coefficients are necessary. However, absolute coupling coefficients are desired in other use cases where absolute amplitudes are required, such as attenuation tomography (De Siena et al., 2014; Hudson et al., 2023b; Reiss et al.,

2022). Here, we briefly introduce two possible ways of estimating absolute coupling coefficients.

The first invokes the assumption that one channel is perfectly coupled to the medium. This channel can then be used as a reference channel and all other channel coupling coefficients scaled relative to this channel. This avoids the need for coincident independent measurements.

The second approach involves having an independent strain measurement of the strain field at one point along the fibre. This could be obtained from two seismometers placed next to the fibre, separated by one gauge-length, for example. This independent strain measurement could be used to calibrate the absolute strain measurement at that point on the fibre, then the other channel coupling coefficients scaled to this measurement. Although this second approach does not make the assumption of perfect coupling of the fibre, it instead assumes that a perfect independent measurement of the strain field can be made, i.e. that the seismometers are perfectly coupled to the medium, for example.

### 2.3 From fibre coupling to medium strain amplitudes

The focus of this work is on quantifying coupling coefficients. However, a key motivation for this is to use DAS for amplitude analysis. The fibre-medium stiffness ratio controls the strain amplitude transfer (Reinsch et al., 2017). Reinsch et al. (2017) apply this to the bonded coatings of the fibre, summing the contributions based on Hooke's law and applying Mohr-Coulomb failure at the fibre-medium interface. Here, we assume elastic coupling as in Celli et al. (2023) and so treat the medium as an additional stiffness to account for. In the simplest case where fibre casing is neglected, the strain in the fibre relative to the strain in the medium for a channel with a coupling stiffness,  $k_m$ , is given by,

$$\varepsilon_f = \frac{k_m}{k_f} \varepsilon_m. \quad (6)$$

In more complex cases, the product of various coupling ratios at interfaces could be considered.

#### 2.3.1 Atmospheric coupling

In the presence of fibre-atmosphere coupling, the system becomes more complex, with atmospheric noise perturbing  $A$  and hence  $C$ . Formally, this can be described by including elastic potential energy terms for atmospheric coupling ( $k_{a,i} \delta x_{a,i}^2, k_{a,i+1} \delta x_{a,i+1}^2$ ) into Eq. 2 and hence also Eq. 4. This perturbs Eq. 4 by adding the additional term,

$$\Delta A_{atmo,i} = \frac{(k_{a,i+1} \delta x_{a,i+1}^2 - k_{a,i} \delta x_{a,i}^2)}{k_f (\delta x_{f,i} + \delta x_{f,i+1}) \delta x_{f,i+1}}. \quad (7)$$

This results in a corresponding additional term in Eq. 5 that corresponds to the atmospheric effect, given by,

$$\Delta C_{i,atmo} = \frac{\Delta A_{atmo,i}}{|A_i|}. \quad (8)$$

Therefore,  $C$  can be artificially underestimated ( $C < 0$ ) or overestimated (with coupling closer to 1 than  $|k_{m,i+1} - k_{m,i}|$  would otherwise give). For example, let us hypothetically imagine that atmospheric coupling is similar to medium coupling ( $k_{m,i}, k_{m,i+1} \simeq k_{a,i}, k_{a,i+1}$ ), but atmospheric displacement is larger than medium displacement ( $\delta x_{a,i} > \delta x_{m,i}$ ). In this case,  $A_i$  is dominated by atmospheric effects and becomes negative, resulting in  $C < 0$ .

Atmospheric coupling that causes  $C < 0$  is acceptable as one can simply define channels with  $C < 0$  as approximately uncoupled to the medium. However, artificial overestimates of coupling are more problematic. One way to reduce this effect is to estimate the coupling over many time-windows within a time-duration where one does not expect fibre coupling to the medium to change. This is because  $\delta x_{a,i}, \delta x_{a,i+1}$  likely vary on timescales far shorter than  $\delta x_{m,i}, \delta x_{m,i+1}$  and so  $(k_{a,i+1} \delta x_{a,i+1}^2 - k_{a,i} \delta x_{a,i}^2)$  will likely vary with a mean near zero, resulting in a mean value of  $\Delta A_{atmo,i}$  and hence  $\Delta C_{i,atmo}$  near zero too.

In the situation where fibre is to some extent coupled to the atmosphere (for example, air-fibre drag or pressure/temperature effects), atmospheric effects become significant when  $k_a \delta x_{a,i}^2 > k_f \delta x_{f,i}^2$ . In practice,  $k_a \ll k_f$  but  $\delta x_{a,i} \gg \delta x_{f,i}$ , so any coupling to the atmosphere is theoretically problematic. Furthermore, there is typically a trade-off with poor fibre-medium coupling and strong fibre-atmosphere coupling. However, atmospheric noise acoustic wavefield likely often breaks the assumption  $\lambda \gg 2x_{ch}$ , and causes  $C$  between channels to be  $\ll 1$ , so it is not expected to significantly effect the reliability of measurement of  $C$ . An obvious inference though is that one should always minimise coupling to the atmosphere by burying the fibre where possible.

#### 2.3.2 Attenuation

In a real-world system, a portion of energy transferred from the medium to the fibre will be attenuated. One way to theoretically describe this attenuation is to define the fibre-medium coupling as visco-elastic. We opt for a Kelvin-Voigt visco-elastic model, assuming that both the elastic and viscous strain-transfer between the medium and the fibre are equal. Such a system can be expressed by,

$$F = k \delta x + \eta \delta \dot{x}, \quad (9)$$

or in energy as,

$$E = \frac{1}{2} k \delta x^2 + \eta \delta \dot{x} \delta x, \quad (10)$$

where  $\eta$  is the viscous damping term. Note that  $\eta$  in this formulation is not strictly viscosity, but rather represents a viscous damping factor in convenient units. This is valid for discrete strain measurements of DAS, since the reference length,  $x_{ch}$ , is constant.

If attenuation is included in the model of Figure 1, then the terms  $\eta_{m,i} \delta \dot{x}_{m,i} \delta x_{m,i}$  and  $\eta_{m,i+1} \delta \dot{x}_{m,i+1}$  are then included in Eq. 4, where  $\eta_{m,i}$  and  $\eta_{m,i+1}$  are the coupling attenuation terms for the  $i^{th}$  and  $(i + 1)^{th}$

channels, respectively. Ignoring geometrical spreading, which is typically negligible over length scales  $x_{ch}$ , this results in a difference in the value of  $A$  due to attenuation of,

$$\Delta A_{attn,i} = \frac{(\eta_{m,i} - \eta_{m,i+1})\delta\dot{x}_{m,i}\delta x_{m,i}}{k_f(\delta x_i + \delta x_{i+1})\delta x_{i+1}}. \quad (11)$$

Note that here, as before, we assume that  $\lambda \gg x_{ch}$ , so  $\delta\dot{x}_{m,i+1} \approx \delta\dot{x}_{m,i}$ . We also assume that atmospheric coupling attenuation is negligible ( $\eta_{atmo} \approx 0$ ). Attenuation results in a perturbation in the coherency coupling coefficient,  $C$ ,

$$\Delta C_{attn,i} = \frac{\Delta A_{attn,i}}{|A_i|}. \quad (12)$$

It is evident from Equations 11 and 12 that the coupling coefficient perturbation is only dependent on the relative attenuation between the two channels. An intuitive observation is that if two channels have the same coupling attenuation ( $\eta_{m,i} = \eta_{m,i+1}$ ), then there will be no change in coupling coefficient between the two channels.

However, the coupling attenuation will also comprise of an absolute term, which should also be calculated if one wants to accurately resolve absolute strain amplitudes. One way to estimate absolute attenuation is to use spectral ratios of the two channels, akin to treating one channel as a virtual source and the other as a virtual receiver. This isolates source and path effects (Hudson et al., 2023b). A brief summary of this is as follows. One first calculates the spectrum of the strain time-series for each channel, for example the Fourier transform,  $\mathcal{F}_i(f)$ ,  $\mathcal{F}_{i+1}(f)$ , or a multi-taper method (Prieto et al., 2009a). The spectral ratio is then taken to remove the virtual source-time function,

$$\begin{aligned} \frac{\mathcal{F}_i(f)}{\mathcal{F}_{i+1}(f)} &= \frac{\mathcal{F}_i(f)}{\mathcal{F}_i(f)e^{\alpha(f)x_{ch}}} \\ &= \frac{1}{e^{\alpha(f)x_{ch}}}, \end{aligned} \quad (13)$$

where  $\alpha(f)$  is the attenuation coefficient describing the absolute attenuation between the two channels. From Aki and Richards (2002),

$$\alpha(f) = \frac{\pi f}{cQ_i(f)} \quad (14)$$

where  $c$  is the phase velocity and  $Q_i(f)$  is the absolute quality factor (the inverse of attenuation). Although the exact phase velocity is unknown, one can assume that it is approximately constant on distances less than the gauge-length,  $L_{gauge}$ . For typical ambient noise wavefields, it is reasonable to set  $c$  to the Rayleigh-wave velocity. If using body-wave signals, then  $c$  could instead be set to that velocity. From this, absolute  $Q$  can be found. One can then quantify the absolute effect of attenuation on  $C$  by considering the energy loss due to the viscous terms in Eq. 10. The quality factor describing attenuation,  $Q$  is defined by Aki and Richards (2002),

$$Q = 2\pi \frac{U}{\delta U} \quad (15)$$

where  $U/\delta U$  is the fractional energy loss between two channels. Since all this loss is accounted for in the viscosity terms, and given that the energy is the work done (i.e.  $U = \int F dx$ ),  $Q(f)$  is found to be,

$$\begin{aligned} Q_i(f) &= 2\pi \frac{c}{x_{ch}f} \left| \frac{\frac{1}{2}k_c\delta x_{m,i}^2 + \eta_{m,i}\delta\dot{x}_{m,i}\delta x_{m,i}}{\eta_{m,i}\delta\dot{x}_{m,i}\delta x_{m,i} - \eta_{m,i+1}\delta\dot{x}_{m,i+1}\delta x_{m,i+1}} \right|. \end{aligned} \quad (16)$$

The amplitude of  $\Delta C_{attn,i}$  can then be estimated.

We provide details of how to attenuation is included in the theoretical model for completeness. However, the approach is involved and so from hereon in, we neglect coupling attenuation.

### 2.3.3 Gauge-length

In practice, DAS interrogators measure phase-shifts of back-scattered light from many defects over a length, referred to as the gauge-length,  $L_{gauge}$ . Therefore, for channel-spacings  $x_{ch} < L_{gauge}$ , the strain measured on a single channel is actually a moving-average overlapping with previous channels. If  $x_{ch} < L_{gauge}$ , then the gauge-length effect affects the relationship between the measured coherency,  $C$ , and  $A$  (see Eq. 5), which is proportional to the coupling along the fibre (see Eq. 4). When including gauge-length, Eq. 5 becomes,

$$C(x) = \sum_{t=0}^{t=t_{win}} \frac{1}{L_{gauge}} \int_{x-L_{gauge}/2}^{x+L_{gauge}/2} \frac{A(x)\varepsilon(x,t)^2}{|A(x)||\varepsilon(x,t)|^2} dx, \quad (17)$$

which can be approximated discretely as,

$$C_i \approx \sum_{t=0}^{t=t_{win}} \frac{1}{L_{gauge}} \sum_{j=i-L_{gauge}/2x_{ch}}^{j=i+L_{gauge}/2x_{ch}} \frac{A_j \varepsilon_j^2 x_{ch}}{|A_j||\varepsilon_j|^2}, \quad (18)$$

Note that the discrete approximation is exactly equal to the continuous function only for  $L_{gauge}|x_{ch}$ . These equations explicitly show how the coherency measurement is affected by multiple neighbouring channels and their corresponding coupling factors. Therefore, it is generally wise to consider quantifying coupling coefficients averaged over the gauge-length.

The gauge-length,  $L_{gauge}$ , also has another potentially important effect on the coupling measurement. It acts as a spatial Nyquist filter, only allowing seismic wavelengths  $\lambda > L_{gauge}/2$  to be resolved. The associated bandwidth limit is  $B < 2c_p/L_{gauge}$ , where  $c_p$  is the velocity of a seismic phase  $p$ . Therefore, any coupling coefficients are only valid for frequencies  $\leq B$ .

### 2.3.4 Frequency dependence

Conventional seismic receivers (seismometers, geophones, etc) typically have frequency-dependent near-surface site effects (Butcher et al., 2020; Shearer and Orcutt, 1987). Recent work has also evidenced near-surface frequency-dependent behaviour in DAS data (Viens and Delbridge, 2024). In our theoretical basis

for coherency-based coupling coefficients, including attenuation via Kelvin-Voigt visco-elastic coupling, introduces a frequency dependence. This is introduced via a rate dependence on the viscosity term ( $\eta$ ) in the stress-strain relationship ( $\sigma = k\varepsilon + \eta\dot{\varepsilon}$ ). In addition to this viscous term that quantifies coupling attenuation, local subsurface frequency-dependent attenuation heterogeneities on the scale of  $x_{ch}$  to  $L_{gauge}$  could perturb coupling-attenuation measurements. Such perturbations are exacerbated by the enhanced sensitivity of strain to shallow subsurface heterogeneities (Capdeville and Sladen, 2024). We cannot isolate shallow subsurface heterogeneity effects from fibre-medium attenuation measurements. However, we suggest that isolation of shallow subsurface heterogeneity effects that are of the same length scale as  $x_{ch}$  to  $L_{gauge}$  is not necessary, since one has to account for both effects in combination in any case. Therefore, for the purposes of pragmatic frequency-dependent coupling quantification, we simply quantify the cumulative frequency-dependent effect of both coupling and any local heterogeneities on scales of  $x_{ch}$ .

### 2.3.5 Abrupt changes in material properties

Our theoretical basis for coupling is deliberately as simplistic as possible, in an endeavour to make it as universally applicable as possible. For example, the method is ambivalent as to whether the medium is a fluid or a solid, albeit with different wave types contributing to the coupling measurement (for example, only coherent P-waves in the fluid case). However, a limitation of this approach is a miscalculation of coupling across abrupt changes in material properties between consecutive channels. Imagine the extreme case where one channel is perfectly coupled to a solid and the next channel is perfectly coupled to a fluid. The coherency of the wavefield between the two channels will be low, since the fluid-coupled channel is only sensitive to P-waves whereas the solid-coupled channel is sensitive to all seismic phases. This will result in an artificial underestimate of coupling since we derive coupling based on inter-channel coherency. This issue only occurs across an abrupt change in material properties on length-scales of the order of the channel spacing or gauge-length (whichever is longer). If material properties change gradually over longer length-scales, then the effects are less significant. There is not a simple solution to this limitation. However, in practice abrupt material contrasts are obvious in DAS data. Where such contrasts are anticipated, one could manually identify their locations independently and then approximate coupling of the affected channels to their neighbouring channels within the same medium.

### 2.4 Finding coherency-based coupling coefficients in practice

The practical implementation of the method used to determine coherency-based coupling coefficients in this work is as follows:

1. Select the time-window(s) within which to use

coherent energy to calculate the coupling coefficients. This could be coherent ambient-noise surface-wave arrivals or direct body-wave arrivals from regional or teleseismic earthquakes. More windows theoretically increases SNR and therefore the accuracy of the coupling measurement.

2. Pre-process, demean, and bandpass filter data within the band of interest.
3. Calculate relative coupling coefficients using the time-windows. Here, we generally calculate coefficients in the time-domain but they can also be calculated in the frequency-domain. In the time-domain, we measure coherency using normalised scalar product between adjacent channels. Alternatively, in the frequency-domain we calculate the convolution, equivalent to the scalar product in the time-domain. In either case, the coherency is maximised based on the optimal lag-time to account for any moveout of the wavefield. Additionally:
  - If the number of adjacent channels is greater than two, then the overall coherency is the average of all window pairs.
  - If one uses multiple windows then the coupling coefficient is the average of the coherency measured for all windows.
4. If absolute coupling coefficients are desired, then a calibrated reference channel is required. This point is addressed in Section 2.2.

## 3 Results and discussion

### 3.1 Overview of datasets

Four datasets are used to explore the performance of the coherency-based coupling quantification method described in this work. A summary of the datasets is given in Table 1. The Gornergletscher and PoroTomo datasets are used to investigate performance of the method, including using different types of coherent wavefields. The coupling coefficient method is then applied to estimate earthquake moment magnitudes for the Rutford Ice Stream and Utah FORGE experiments.

### 3.2 Coherency-based coupling quantification performance

First, we use two of the real-world datasets to investigate the validity of coherency-based coupling measurements in practice.

Secondly, we use a regional earthquake arrival at the PoroTomo experiment (Feigl et al., 2016; Wang et al., 2018) to compare how well the ambient noise field quantifies coherency between channels relative to direct body-wave arrivals.

#### 3.2.1 Evidence that coherency can discriminate between well-coupled and poorly-coupled channels

Data from Gornergletscher, Switzerland (Hudson et al., 2025), provide an ideal example for how well a

Experiment	Interrogator	$x_{ch}$	$L_{gauge}$	$f_s$	$L_{fibre}$	Further details
Gornergletscher, Switzerland	Sintella ONYX	1.6 m	6.4 m	1000 Hz	1.2 km	Hudson et al. (2025)
PoroTomo experiment, USA	Silixa iDAS	1.0 m	10 m	1000 Hz	8.4 km	Wang et al. (2018)
Rutford Ice Stream, Antarctica	Silixa iDAS	1.0 m	10 m	1000 Hz	1.0 km	Hudson et al. (2021)
Utah FORGE experiment, USA	Silixa Carina	1.0 m	10 m	2000 Hz	1.0 km	Lellouch et al. (2021)

**Table 1** Overview of datasets used in this study. For further details, see the suggested literature.  $f_s$  is sampling rate and  $L_{fibre}$  is the fibre length.

coherency-based metric quantifies coupling, since 1 km of fibre was initially laid on the ice surface before melting and freezing in a few cm below surface 12 hours later. The fibre therefore transitioned from poorly-coupled to well-coupled to the subsurface. Furthermore, a section of the fibre was deployed in a crevasse field (see Figure 2c,d), resulting in some sections of fibre being approximately permanently uncoupled from the medium. To quantify coupling along the fibre, two one minute windows of data are randomly selected, one during each time period. These contain only ambient noise, with no identifiable seismicity.

Results are shown in Figure 2. When the fibre is frozen-in, the mean coupling coefficient increases while the variance in coupling coefficient visibly decreases relative to the initial, hypothetically poorly coupled fibre. The majority of channels for the frozen-in time period have coupling coefficients  $> 0.8$  (1 equates to perfect relative coupling between channels). Technically since it is a relative measurement, relative coupling coefficients of 1 could also equate to perfectly uncoupled neighbouring channels, but we rule out this behaviour here since post freeze-in inspection suggests that channels are well-coupled, with the exception of single channels ( $< 1.6$  m) overlying open crevasses. The fibre between the interrogator and the start of the crevasse field exhibits high levels of consistent coupling, as expected since the fibre here is almost always in contact with the ice. This is in contrast to the fibre within the crevasse field, which exhibits significantly higher variance, with specific, short sections (1 to 2 channels) of the fibre having coupling coefficients decreasing to  $\sim 0.5$ .

The two observations from these results that provide us with the most confidence that a coherency-based metric can quantify fibre coupling are: (1) the mean increase and variance decrease after the fibre freezes into the medium; and (2) the observation of poor coupling on single, isolated channels only within the crevassed region. As the fibre freezes in, if it becomes well coupled to the subsurface then any coupling metric should typically increase, as observed in the mean coupling of Figure 2b compared to Figure 2a. However, for some channels the coupling coefficient decreases. We interpret this to be a consequence of the fibre being well coupled to the atmosphere during the time period of Figure 2a, with channels of high coherency due to coherent atmospheric noise. This interpretation is further evidenced by the reduced variance observed in Figure 2b compared to Figure 2a. Coherent atmospheric signals (for example, wind) would typically act on wavelengths of only a few channels, leading to the higher

levels of variance observed in Figure 2a. We know that certain channels are poorly coupled within the crevasse region (see Figure 2d). Low coupling coefficients on isolated channels within the crevasse field in Figure 2b provide us with confidence in the fidelity of the coherency-based coupling method to represent both well and poorly coupled channels, at their expected locations. Theoretically, consecutive perfectly isolated, uncoupled channels would have coupling coefficients of 1, but since only one to two channels overly individual crevasses and these channels are somewhat coupled to the atmosphere, we expect these channels to have near-zero coupling coefficients. However, their significantly non-zero values ( $> 0.5$ ) are likely primarily due to gauge length effects. The gauge length of this experiment is 6.4 m, whereas the fibre over crevasses is typically decoupled for  $\sim 0.5$  m, only a fraction of the total averaged coupling measurement. A further encouraging result is that we generally do not observe high variance in the crevassing region after excluding particularly poorly coupled channels that traverse crevasses, even though the different linear sections of fibre are sensitive to noise from different azimuths and intrinsic attenuation and scattering from subsurface fractures are prevalent. This suggests promise for using coherent noise to quantify coupling in other highly fractured environments.

While the results of Figure 2 evidence that coherency-based coupling measurements can provide quantitative estimates of coupling, the results are not perfect. One might expect frozen-in fibre to have coupling coefficients of approximately one. We attribute lower-than-expected coupling coefficients to be caused by several factors. Firstly, both instrument and short-wavelength ( $\lambda < x_{ch}, L_{gauge}$ ) atmospheric noise can reduce coherency between channels. Reducing the effect of instrument noise is possible (Chen et al., 2022; Lapins et al., 2023; van den Ende et al., 2023; Yang et al., 2023) but not applied here. Isolating surface fibre from atmospheric noise is challenging, although direct burial of fibre would reduce such noise considerably, with negligible gains found for conventional receivers buried  $> 0.4$  m (Naderyan et al., 2016). Another unknown is quantifying the effect of any remaining subsurface heterogeneity or topographic curvature on length scales  $< L_{gauge}$ . These are effects that are challenging to compensate for. However, in another dataset presented in this work, we do remove channels exhibiting high curvature from the analysis (see Figure 3). A further limitation is not having sufficient incident coherent ambient noise across a wide bandwidth (in this case 1 to 100 Hz). As the frequency increases, its sensitivity to hetero-

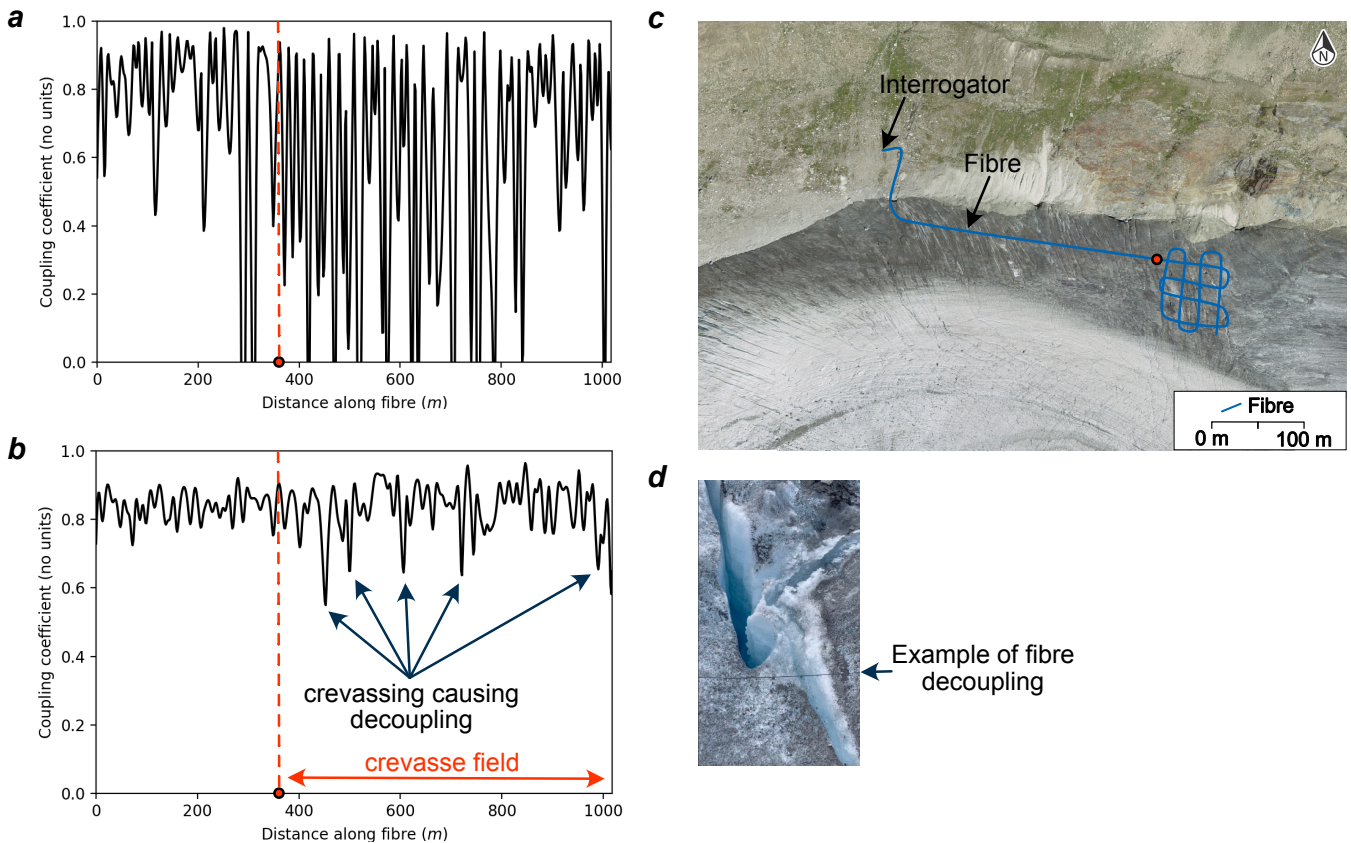


**Figure 2** Example of coherency-based coupling quantification performance. Data are from a fibreoptic deployment on Gornergletscher, Swiss Alps, in October 2023. a. Coupling coefficient vs. distance along fibre before fibre was frozen to the glacier surface (17:00, 18<sup>th</sup> October 2023). b. Coupling coefficient vs. distance along fibre after melt-in and subsequent freeze-in (10:00, 19<sup>th</sup> October 2023). c. Approximate geometry of the fibre. Red dot corresponds to red dashed lines in (a,b). d. Example of fibre decoupled from the ice at a crevasse. Coupling coefficients in (a,b) are calculated from 1 to 100 Hz and using a channel window length of three. The aerial imagery in (c) is from the Federal Office of Topography (Swisstopo).

geneties of shorter spatial scales increases, yet so does attenuation. Therefore, our coupling measurements are likely dominated by lower frequency coupling behaviour. A final limitation noted here is channel window length, that is the number of channels over which the cross-correlation coherency measurement is made. Here, we set this to approximately the gauge length. Wider windows result in more consistency along the fibre, but inevitably dampen the effect of any small-scale heterogeneities, for example the crevasses, yet also decreasing the influence of any single, approximately perfectly coupled channels.

### 3.2.2 Coherent reference wavefield from ambient noise vs. body-waves

In the glacier example, we use the ambient noise wavefield to quantify the coupling coefficients along the fibre. However, in doing so we assume that sufficient coherent energy exists within the noise wavefield to allow coupling to be calculated. To test this assumption, we show results from a regional earthquake recorded at the PoroTomo experiment (Feigl et al., 2016; Wang et al., 2018) (see Figure 3a). The regional earthquake is ~ 150 km SSE of the deployment and so body-waves should exhibit minimal amplitude coherency variations due to radiation pattern effects. One can therefore use

body-waves from such an earthquake to quantify coupling instead of ambient noise. Body-waves from the earthquake arriving at the fibre are shown in Figure 3b. Coupling coefficients calculated using both body-waves as well as single and stacked ambient-noise windows independently are shown in Figure 3c.

The results show that body-wave derived coupling coefficients have a lower variance than the ambient-noise derived coupling coefficients (see Figure 3d,e). Body-wave coupling coefficients are also close to one for the majority of channels, suggesting uniform coupling along the majority of the fibre. Noise-derived coupling coefficients are lower, interpreted as likely due to a lower ambient-noise to instrument-noise ratio. Given that these single noise-window values have significantly higher variance and lower amplitude than the Gornergletscher coupling coefficients, we at least partially attribute the poorer ambient-noise coupling coefficients in Figure 3 to lower ambient-noise amplitudes at the study site. Differing instrument noise amplitudes could also make a contribution. However, noise-derived coupling coefficients using 5 random stacked windows significantly reduces variance in coupling coefficient (red line, Figure 3c,d), allowing one to consistently identify poorly coupled channels (coupling coefficient < 0.5) using either body-waves or ambient-noise. For example, the two adjacent channels shown in Figure 3e are cor-

rectly identified as having poor and good coupling by both body-wave and ambient-noise data. A further observation is that, regardless of data used, the coupling coefficients are approximately insensitive to fibre curvature. This is partly because we remove sections of the fibre with high curvature, but also presumably because the different fibre orientations are generally sensitive to the body-wave arrivals and any dominant ambient-noise sources.

In summary, the results of Figure 3 show that ambient-noise derived coupling coefficients can identify well and poorly coupled sections of fibre, although body-waves provide higher contrasts between high coupling coefficient and low coupling coefficient channels, aiding identification of poorly coupled channels. However, suitable body-waves are not always present, due to experiment duration and/or if coupling varies temporally faster than observable regional or teleseismic earthquake rate. Ambient-noise is always present and our results show that it can be used to measure coupling coefficients that closely agree with body-wave derived values. Stacking multiple windows is critical for achieving such performance, with more noise windows increasing the ambient-noise to instrument-noise ratio, similar to stacking techniques used to boost SNR ambient-noise interferometry or tomography (Yang et al., 2022).

### 3.3 Application to moment magnitudes

One example in seismology where absolute amplitude information is important is the calculation of seismic moment release of an earthquake. We use seismic moment calculations to explore the importance of quantifying coupling and evidence the benefits that unlocking amplitude information can provide. We show moment magnitude ( $M_w$ ) results for two datasets in order to assess the importance of quantifying coupling for absolute amplitude analysis. One dataset is a surface deployment at Rutford Ice Stream, Antarctica (Hudson et al., 2021). The other is a downhole geothermal dataset from the Utah FORGE geothermal experiment, USA (Lellouch et al., 2021).

#### 3.3.1 Calculating seismic moment

To calculate moment magnitudes, we first quantify any variations in coupling and apply corrections to all channels. We use the highest relative coupling coefficient channel as a reference channel and convert all relative coupling coefficients to absolute values relative to this channel. Second, we convert from strain-rate to displacement via direct integration, removing any high-curvature sections of fibre beforehand. Specifically, this involves one integration in each of the space and time domains and is only valid along approximately linear sections of fibre (see Hudson et al. (2025) for more details). We favour this method partly since infinite apparent velocity integration noise can be removed with an fk-filter, but more importantly because unlike other methods, it does not require a reference seismometer (Lindsey et al., 2020). We then fit a Brune model to

the displacement spectra (Brune, 1970) using a spectral-ratio method to isolate source and path effects (Hudson et al., 2023b). We then use the long-period spectral level derived from the optimal Brune model to calculate seismic moment (Stork et al., 2014) before converting from seismic moment to  $M_w$  using the scale of Hanks and Kanamori (1979).

#### 3.3.2 Moment magnitude results

Seismic moments for one icequake are explored in detail in Figure 4. This icequake contains no discernible P-wave energy due to the presence of a steeply-varying shallow firn layer velocity gradient, but strong S-wave energy generated by shear of the ice sliding over the underlying bed (Hudson et al., 2021). We calculate seismic moment for every channel independently, as well as the mean moment, both with and without a coupling correction applied. We correct for radiation pattern effects using the best-fitting double-couple moment tensor found in Hudson et al. (2021). The coupling correction is applied by first calculating the coupling coefficients of each channel along the fibre using the noise window shown in Figure 4a. The channel with the highest coupling coefficient is assumed to be approximately perfectly coupled and set as a reference channel, with all other seismic moments scaled by their coupling coefficient relative to that of the reference channel. The results are shown in Figure 4b. Although there is some variation between channels, both the uncorrected and coupling-corrected mean seismic moments are close to the moment calculated using a coincident geophone. Applying the coupling coefficient correction marginally increases the mean moment, taking it closer to the geophone reference value. However, this increase is within the uncertainty in seismic moment (see Figure 5). There is significantly more variation in seismic moment between channels than in the difference between uncorrected and coupling-corrected values. The coupling coefficients along the fibre do not correlate with this variation in seismic moment (Figure 4c), which implies that the variations are not coupling related. Instead, we interpret variations in seismic moment between channels to be some combination of regions of firn with a heterogeneous attenuation structure (Agnew et al., 2023) and/or anisotropy (Hudson et al., 2021, 2023a; Kufner et al., 2023). Although we correct for radiation pattern amplitude variations, uncertainty in the moment tensor solution means some channels near nodal planes may have S-wave amplitudes dropping close to or below the noise level, possibly further contributing to variations (see Hudson et al. (2021) for moment tensor inversion of the event). In summary, we suggest that other factors perturb observed strain-rate amplitudes significantly more than coupling, at least in this instance.

The icequake in Figure 4 is also used to briefly investigate how coupling varies with frequency. Figure 4c shows coupling coefficients calculated for four frequency bands in the time-domain, as well as calculating coupling coefficients in the frequency-domain. Firstly, the coupling coefficients calculated in the time and frequency domains are in close agreement, con-

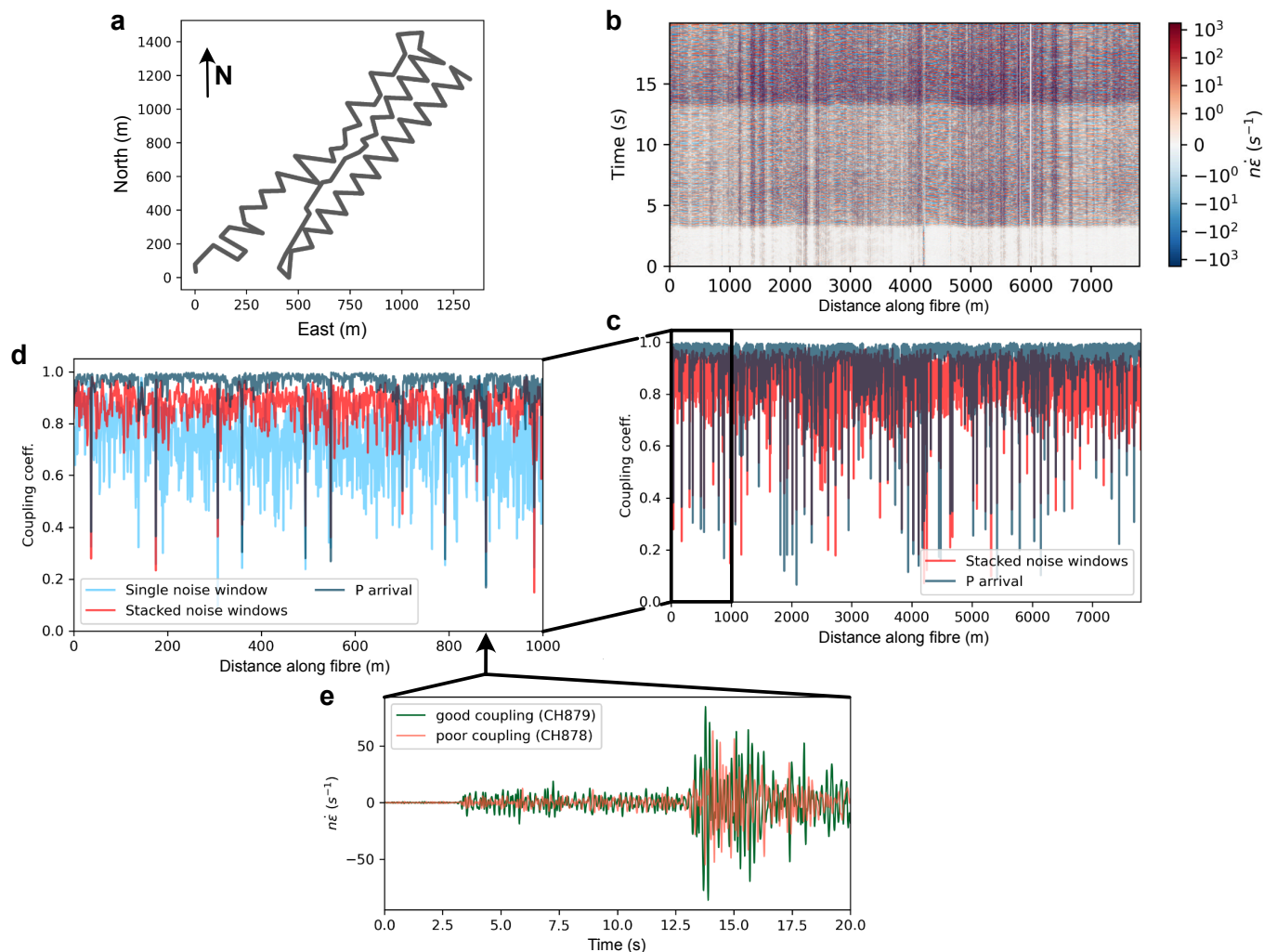


**Figure 3** Comparison of body-wave vs. ambient-noise field for calculating coupling coefficients from the PoroTomo experiment (Muir and Zhan, 2021). a. Fibre geometry. b. Waveforms observed along the fibre from a regional event occurring on 21<sup>st</sup> March 2016, approximately 150 km SSE of the deployment. c. Coupling coefficients calculated along the whole fibre using body-waves (dark blue) and ambient noise (light blue). d. Same as (c), but for a small portion of the fibre and with noise stacked using 5 random time windows. e. Example seismograms of two channels identified as well-coupled and poorly-coupled to the medium. Note that channels near corners of the fibre are removed. Coupling coefficients are calculated in the frequency-domain.

firming the equivalence of quantifying coupling in either domain. The results for coupling  $> 10$  Hz in this case are also all in close agreement, with significant variations only observed for the 1 to 10 Hz frequency band. In some instances, this variation is likely real (for example, at  $\sim 825$  m), where the majority of observations show a decrease in coupling. However, in other cases, we attribute strong variations to not using a sufficiently long window to adequately resolve low frequency coupling. This is important since long-period spectral levels are used for estimating seismic moment. We come to this conclusion partially based on our window length, but also because we would expect poor coupling at lower frequencies (longer wavelengths) to also be exhibited at higher frequencies (shorter wavelengths), but not vice versa. Overall, the results suggest that at least if one wishes to estimate coupling over a broad frequency range, then the results are stable.

Figure 5 shows estimated DAS-derived moment magnitudes compared to geophone-derived moment

magnitudes for icequakes from Rutford Ice Stream and earthquakes from the Utah FORGE experiment. The icequake geophone-derived magnitudes are calculated using a geophone coincident to the fibre and the FORGE earthquake magnitudes are calculated using a string of borehole geophones in the same monitoring well. The majority of events from both datasets fall upon the 1 : 1 line, within uncertainty. Exceptions to this are some of the smallest events and the very largest event. In these cases, it is likely that the uncertainty in  $M_w$  from the DAS and/or the geophones is underestimated (note that we do not have uncertainty estimates for geophone-derived  $M_w$  due to single-instrument measurement or no third-party data availability). In any case, the results show that it is unlikely that coupling corrections could cause such a discrepancy. Indeed, all coupling corrected  $M_w$  estimates lie within the uncertainty of their uncorrected counterparts. We gain further confidence in the coupling coefficient method from the observation that coupling correction has negligible

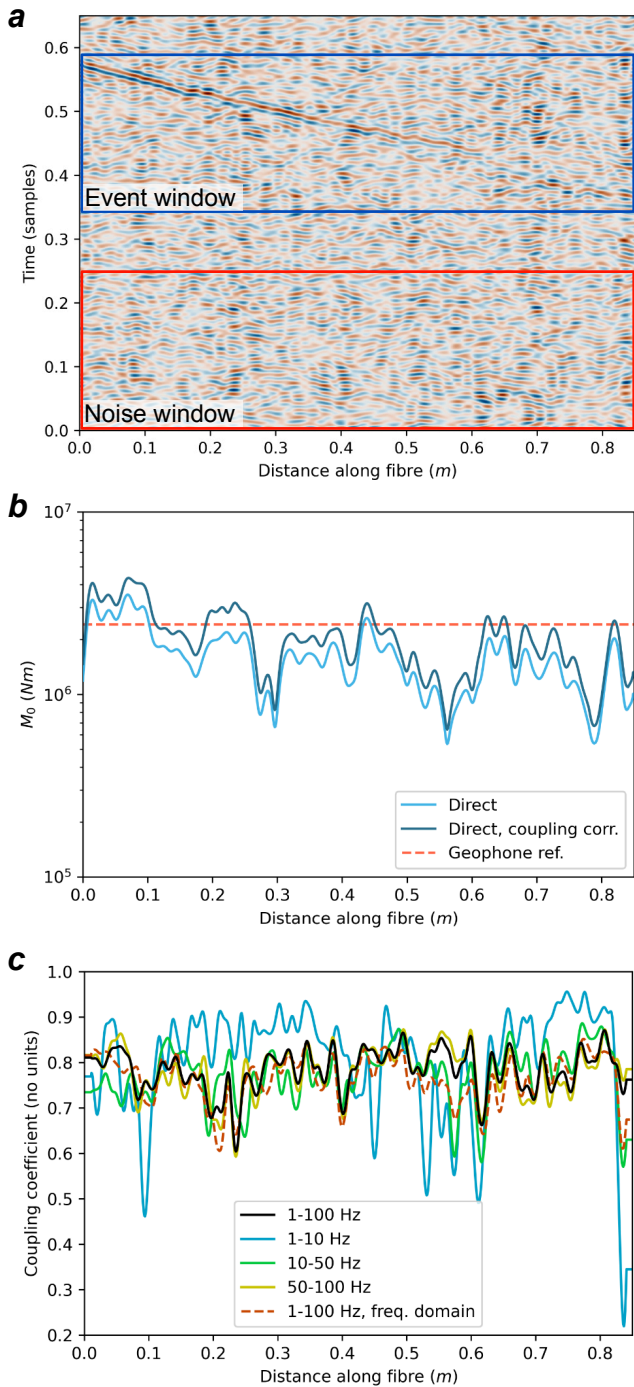


**Figure 4** Example of Antarctic icequake, including seismic moments and coupling coefficients within different frequency bands along a fibre. a. Example of icequake signal, including the event window and the noise window used to calculate the coupling coefficients. b. Seismic moment with distance along the fibre, with and without the coupling correction. Red dashed line shows the reference seismic moment calculated using a coincident geophone. c. Coupling coefficients calculated in the time-domain for four different frequency bands, along with coupling coefficients calculated in the frequency-domain for the 1 – 100 Hz band. More information on the icequake can be found in Hudson et al. (2021).

difference on the FORGE earthquake magnitudes. For this dataset, the fibre is cemented into the well and so

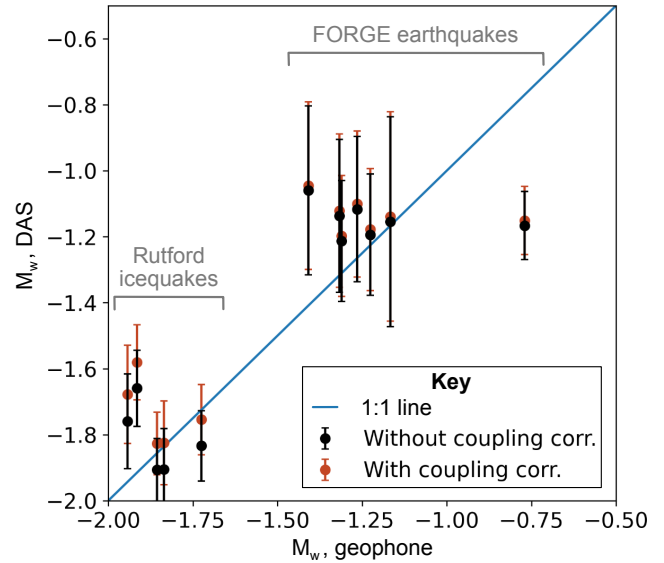


**Figure 5** Seismic moment magnitude ( $M_w$ ) estimated from DAS compared to geophones for two datasets: icequakes from Antarctica (see Hudson et al. (2021) for further details); and earthquakes from the Utah FORGE geothermal experiment (see Lellouch et al. (2021) for further details). Coupling corrections applied here are derived from single coupling coefficients per channel within a bandwidth of 1–100 Hz

coupling should be as perfect as is practically feasible.

Together, the results of Figures 4 and 5 emphasise that at least in some cases, it is likely that coupling does not pose a significant source of uncertainty for using DAS for amplitude-based measurements. Together with the other two datasets in this study, our findings suggest that simple, pragmatic coherency-based coupling coefficients can be used to at least identify well-coupled and poorly-coupled channels. This raises the open question of whether it might be valid to assume and apply an approximately binary distribution of coupling coefficients in fibreoptic experiments going forward.

### 3.4 Applicability, limitations and alternative approaches

#### 3.4.1 Applicability

The strengths of the coherency-based coupling coefficient method presented here lie in it being a data-driven method that is underpinned by a theoretical basis. Being data-driven, the method can be applied to any DAS dataset without the need for any coincident complementary instrumentation and does not require precise knowledge of fibre geometries (with the exception of high curvature sections, see Section 3.4.2). Relating the data-derived coherency measurements to an underlying physics-based analytical model allows one to understand the key factors that affect coupling and the origins of uncertainty in any coherency-based coupling measurement. This physical model is deliberately as simplistic as possible, in order to capture the key concepts in a first-order fashion. We therefore wish to empha-

size that this method does not capture the full physics describing the system, but is sufficient to start harnessing amplitude information from DAS measurements.

The most simple and general application of DAS coupling coefficients is identifying poorly coupled channels. One of the greatest benefits of DAS is that the spatial sampling density provides some data redundancy in many situations. Therefore, one can typically afford to remove or down-weight noisy, poorly coupled channels.

Our results show that coupling coefficients can be used to correct for coupling variations for calculating earthquake magnitudes. Calculating earthquake magnitudes is critical for any seismic monitoring, in particular induced seismicity from industrial activities such as geothermal energy production or carbon capture and storage (Edwards et al., 2015; Grandi et al., 2017; Grigoli et al., 2017; Lellouch et al., 2021; Lellouch and Biondi, 2021). While our results suggest that coupling is not a significant source of uncertainty when calculating earthquake magnitude, it may become important for dark-fibre deployments or subsea deployments where one has little control over coupling (Fernandez-Ruiz et al., 2022; Igel et al., 2024; Sladen et al., 2019).

There are numerous other passive seismology applications that require or benefit from absolute amplitude measurements. Attenuation tomography is one application, whether using body-waves (De Siena et al., 2014; Hudson et al., 2023b; Reiss et al., 2022) or surface-waves (Lawrence and Prieto, 2011; Liu et al., 2021). Fibreoptic sensing with coupling effects quantified could provide orders-of-magnitude greater receiver spatial sampling, improving tomography resolution, especially in the shallow subsurface. Another application is moment tensor inversion. For example, Hudson et al. (2021) performed full-waveform moment tensor inversion of icequakes, making the assumption of perfect coupling along the entire fibre. While this assumption is approximately valid in that case, quantifying coupling would provide greater constraint of such inversions, especially in more geologically complex scenarios (Lecoulant et al., 2023). Gains could also be made for first-motion polarity moment tensor inversions (Li et al., 2023), where poor-coupling could artificially damp low-amplitude first-motions leading to incorrect first-motion identification.

There are also active seismology applications. One example is AVO studies (Castagna, 1993; Ostrander, 1984). AVO is where amplitude variations of a seismic wave reflecting off an interface are measured with offset. Varying the offset varies the angle of the wave with the interface, varying the transmission and reflection coefficients. These coefficients vary with material property changes at the interface, such as porosity and the properties of any pore fluids (Ostrander, 1984). Our method of obtaining DAS amplitude information may therefore allow DAS measurements to be used for AVO analysis if the sensitivity of strain measurements to local heterogeneities is not prohibitive (Capdeville and Sladen, 2024).

### 3.4.2 Limitations and further refinement

The coupling quantification method presented here relies on the assumption that a coherent wavefield exists on length scales of multiple DAS channels. The minimum requirement of our method is that the change in displacement ( $\propto$  strain) is constant at a given point in time for two neighbouring channels in the medium adjacent to the fibre. This assumption is a fundamental limitation that one cannot avoid. While this coherency assumption likely holds in the majority of cases, there are instances where it does not hold. One such instance is the case where the fibre has significant curvature on length scales less than the inter-channel distance or gauge-length. Here, even if the wavefield is coherent over multiple channels, the sensitivity of the fibre to the wavefield will vary, causing an underestimation in the coupling coefficient over these channels (Martin, 2018). For most applications, we do not deem this an issue in practice, since it is straight-forward to remove such channels from analysis. Such channels are likely not useful for other analyses in any case. A further instance where the coherency assumption may be limiting is using more than two channels to calculate coupling. In some instances, it may be beneficial to compare the coherency of more than two consecutive channels, especially if  $x_{ch} \ll L_{gauge}$ . Using too many consecutive channels will break the coherency assumption, especially for shorter wavelengths. Similarly, using only two consecutive channels over windows with low coherent noise amplitudes compared to instrument noise may lead to poor estimates of inter-channel coherency. Both situations would result in underestimating coupling coefficients. A further limitation arising from the coherency assumption is the dependence on frequency. Higher frequency components of the seismic wavefield will have shorter wavelengths. At some point, the wavelength will become sufficiently short that it will break the coherency assumption. This limit is easily calculated and coupling coefficients should not be applied to analysis of such signals.

Small-scale, local near-surface heterogeneities may also break the coherent wavefield assumption in certain circumstances. It has been shown that even for changes in elastic properties of the medium on scales smaller than the wavelength, the strain wavefield measured by DAS can be significantly perturbed compared to the velocity wavefield measured by conventional receivers (Capdeville and Sladen, 2024). This is because these heterogeneities can cause local interference of the wavefield, perturbing the wavefield gradient (or strain). The numerical modelling results of Capdeville and Sladen (2024) suggest that strong isolated heterogeneities, such as stones in unconsolidated soil, could significantly alter the coherency of the wavefield between channels. While this effect could be important at certain sites if one uses direct body-wave signals as the reference wavefield, the effect is likely less important if using an ambient noise reference wavefield to estimate coupling. This is because the ambient noise wavefield is highly scattered, and therefore energy arrives at many incidence angles relative to the fibre, reducing directional

effects of any local, small-scale heterogeneities. Furthermore, such local heterogeneities are likely not isolated, but are randomly distributed with a distribution of sizes. This distribution may diffuse interference effects, having less impact on wavefield coherency and therefore coupling estimates. Overall, we find that at least for the real-world datasets analysed here, local small-scale heterogeneities do not play a significant role in perturbing coupling measurements. However, this is an effect to be cautious of, especially in settings with non-randomly distributed heterogeneities and/or when using direct-wave reference wavefields.

Common mode noise may also cause issues. This is noise due to the interrogator itself moving, causing a coherent apparent arrival simultaneously across all receivers. Common mode noise would cause artificial overestimates of coupling coefficients. However, identification of windows containing significant common mode noise is straight-forward, and could be removed using an fk-filter if required, similar to that applied to remove integration noise in [Hudson et al. \(2025\)](#).

A further challenge is that fibre-medium coupling is frequency dependent. This frequency dependence originates from various factors including coupling attenuation as well as channel-spacing and gauge-length effects. The theoretical basis we present, which holds for frequency-dependent effects arising from attenuation and relevant theory for the sensitivity of gauge-length to frequency, is eloquently described in [Martin \(2018\)](#). Several ways of quantifying frequency dependent coupling coefficients are to apply narrow Gaussian bandpass filters in the time-domain or to measure coherency in the frequency-domain. However, we have not explored non-linear elastic effects ([Delsanto, 2006](#); [Ostrovsky, 1991](#)) on coherency theoretically. Therefore, we do not know whether frequency-dependent coupling coefficients measured at different frequencies are valid in the presence of a non-linear elastic medium.

Isolating fibre-medium coupling attenuation from near-surface attenuation represents a further challenge. Often, the near-surface may comprise unconsolidated material that may have a particularly low quality factor (high attenuation) relative to the majority of the medium. At length-scales less than the gauge-length, sufficiently resolving near-surface attenuation to isolate it from coupling attenuation is likely impossible. Assuming this is the case, then we suggest a pragmatic approach of simply measuring coupling and near-surface (sub-gauge-length) attenuation together, rather than attempting to isolate them. Although this may limit near-surface imaging studies, it still allows one the possibility to quantify attenuation in the majority of the medium. Similarly, this approach also means one would not strictly measure coupling attenuation alone. However, in reality all seismic waves incident at the fibre have to pass through an attenuative near-surface layer, so practically one might as well quantify that too.

A final limitation of note is that the method requires coherent wave sources incident at the fibre that are independent of the seismic signals that one wishes to analyse post-coupling quantification. Here, we show how both ambient-noise wavefields and regional (or

teleseismic) wavefields can be used to quantify coupling. Ambient-noise wavefields are present at all times and locations on Earth, although the amplitude varies, and so stacking of multiple noise windows is likely required to obtain sufficiently accurate coupling estimates. Large magnitude regional or teleseismic arrivals are not always present, but if they are, our results suggest that these may provide better coupling coefficient estimates. An unexplored question is what type of wavefield would be optimal in subsea environments. In subsea environments, oceanic microseisms may be more complex, especially in coastal settings. Also, coupling in subsea deployments may also vary significantly temporally due to ocean currents moving sediment and tides varying hydrostatic pressures, limiting the use of regional or teleseismic arrivals. However, if coherent wavefields are present, then the coupling quantification method presented here will be applicable.

Here, we approach the DAS coupling problem in a pragmatic way, seeking to estimate fibre-medium coupling on any real dataset in a practically applicable way, with as simple a theoretical foundation as possible. However, although we evidence that the method works for the examples shown, useful future work would be to further explore the problem using numerical modelling ([Celli et al., 2023](#)) applied to controlled laboratory experiments ([Wuestefeld et al., 2021](#)).

### 3.4.3 Comparison to alternative approaches

Alternative methods that can extract coupling information exist. These fall into two categories: physics-informed numerical modelling of DAS response and using coincident conventional receivers to calibrate DAS response. Both methods effectively capture some form of coupling information in that they quantify the transfer of true strain in the medium to strain observed in the fibre. Here, we discuss the merits and limitations of such approaches compared to the method described in this work.

Physics-informed numerical modelling is a promising technique where one attempts to simulate the full response of each fibre channel to deformation of the medium. One example of this is the work of [Celli et al. \(2023\)](#), who use elastic lattice particle modelling to describe both coupling of the fibre to the medium and frequency response. Such a model can describe many of the theoretical considerations described in [Reinsch et al. \(2017\)](#) and [Hubbard et al. \(2022\)](#). It also inspired the theoretical basis of this work. One could attempt to estimate coupling along a fibre by setting up a numerical simulation of a real-world experiment as accurately as possible. Then, the results of the simulation could be compared to the real-world response, perhaps via a formal inversion. If the majority of first-order effects were captured in the model, then the result would be similar to our approach, with system noise playing the same limiting role. The benefit of this approach would be obtaining absolute estimates for all the coupling stiffnesses directly, whereas our method only quantifies coherency, which is a net effect of a number of coupling behaviours combined. The frequency re-

sponse due to coupling could then be estimated using physics-constraint rather than empirically. One would also obtain the full instrument response rather than just the effect of coupling. The challenges of such an approach would be the complexity of an inversion (number of free parameters) and the risk of not capturing some real-world effect adequately in the model.

The other alternative method is using coincident conventional receivers to calibrate DAS response. Like our approach, this is data-driven. There are various ways to obtain the full response of the fibre, but two promising ways are described by [Lindsey et al. \(2020\)](#) and [Muir and Zhan \(2021\)](#). [Lindsey et al. \(2020\)](#) use DAS strain observations combined with velocity observations and instrument response of coincident seismometers to deconvolve the DAS instrument response. This method quantifies the full transfer function as a function of frequency, including coupling effects. However, it is limited by the availability of coincident receivers and the assumption that those instruments are perfectly-coupled to the medium. The second approach is to use a network of conventional receivers to observe the seismic wavefield and reconstruct the wavefield that should be observed by the DAS fibre ([Muir and Zhan, 2021](#)). A strength of this method compared to that of [Lindsey et al. \(2020\)](#) is that it does not require coincident receivers, but a limitation is that it requires a number of receivers in the same local region as the fibre, spaced suitably for capturing and reconstructing the wavefield across the entire DAS fibre. A further limitation of the method of [Muir and Zhan \(2021\)](#) is that only certain frequency components of the wavefield can be precisely reconstructed, leading to amplitude differences at other frequencies. The strength of both these data-driven methods compared to the method presented here is that they can quantify the full instrument response, at least for some sections of the fibre. However, the critical limitation of these methods is that they require coincident receivers that adequately observe the wavefield.

Given the performance of the alternative methods described above, we suggest that for best possible results, one might decide to combine approaches to optimally describe coupling along entire fibreoptic deployments. However, if one only records DAS data, then the method presented in this work provides the simplest means to estimate fibreoptic coupling coefficients.

## 4 Conclusions

Quantifying coupling of fibre to the medium is essential for unlocking amplitude analysis of DAS data. Here, we present a pragmatic way to estimate coupling coefficients using a coherent reference wavefield (either ambient-noise or body-waves). We provide a theoretical basis justifying the link of coherency to fibre-medium coupling. The method requires no complementary data, at least for relative coupling quantification, so is applicable for any DAS dataset. However, it should be noted that there are also limitations of the method. These include coherency coupling estimates not being possible for sections of fibre with high curvature and the possibility of local, small-scale hetero-

geneities perturbing the inter-channel coherency of the strain wavefield in certain instances.

Results confirm that the method can identify well-coupled channels from poorly-coupled channels and that either ambient-noise or direct body-wave wavefields can be used to quantify coupling. Results using the method to correct for coupling effects when calculating seismic moment suggest that coupling may not be as important as commonly assumed. To first-order, results suggest that fibre coupling may be approximated in a binary way: either poorly-coupled and so assume zero coupling or well-coupled and assume approximately perfect coupling.

The method and associated theory described here, along with other recent work ([Celli et al., 2023](#); [Lindsey et al., 2020](#); [Muir and Zhan, 2021](#); [Reinsch et al., 2017](#)), unlock the use of amplitude information from DAS measurements and provide a foundation for more comprehensive description of coupling going forward.

## Acknowledgements

We thank the editor W. Wu, the reviewer Y. Capdeville, and an anonymous reviewer for their comments that no doubt improved the manuscript. We also thank collaborators who helped collect various data used to test the method developed in this work. For the Antarctic dataset, they were A. Brisbourne, JM. Kendall and S. Kufner. For the Gornergletscher dataset, they were F. Walter, E. Wolf, R. Cross and E. Julen. We thank Silixa for loan of the DAS interrogator used for the Antarctic deployment. Furthermore, we thank P. Edme for insightful discussions that no doubt improved the manuscript. This work was funded by a Leverhulme Early Career Fellowship (ECF-2022-499) and Oxford University's John Fell Fund (0013666). A philanthropist kindly provided logistical support through use of a vehicle for the Gornergletscher fieldwork.

## Data and code availability

DAS recordings and associated data used in this study from Gornergletscher and Rutford Ice Stream are deposited in a perpetual online repository ([Hudson, 2024](#)). DAS recordings and associated data from the Porotomo experiment are available open-access via an online repository ([Feigl et al., 2016](#)). DAS recordings and associated data from the Utah FORGE geothermal experiment are also available open-access from US DOE Geothermal Data Repository ([Martin and Nash, 2019](#)).

## Competing interests

There are no competing interests for any of the authors. Although one author is currently an employee of a DAS interrogator manufacturer, the research and findings of this paper are entirely independent.

## References

- Agnew, R. S., Clark, R. A., Booth, A. D., Brisbourne, A. M., and Smith, A. M. Measuring seismic attenuation in polar firn: method and application to Korff Ice Rise, West Antarctica. *Journal of Glaciology*, page 1–12, Oct. 2023. doi: 10.1017/jog.2023.82.
- Aki, K. and Richards, P. G. *Quantitative Seismology*. University Science Books, 2002.
- Brune, J. N. Tectonic stress and the spectra of seismic shear waves from earthquakes. *Journal of Geophysical Research*, 75(26): 4997–5009, Sept. 1970. doi: 10.1029/jb075i026p04997.
- Butcher, A., Luckett, R., Kendall, J.-M., and Baptie, B. Seismic Magnitudes, Corner Frequencies, and Microseismicity: Using Ambient Noise to Correct for High-Frequency Attenuation. *Bulletin of the Seismological Society of America*, 110(3):1260–1275, Apr. 2020. doi: 10.1785/0120190032.
- Capdeville, Y. and Sladen, A. DAS sensitivity to heterogeneity scales much smaller than the minimum wavelength. *Seismica*, 3(1), Jan. 2024. doi: 10.26443/seismica.v3i1.1007.
- Castagna, J. P. Petrophysical imaging using AVO. *The Leading Edge*, 12(3):172–178, Mar. 1993. doi: 10.1190/1.1436939.
- Celli, N. L., Bean, C. J., and O'Brien, G. S. Full-waveform simulation of DAS records, response and cable-ground coupling. *Geophysical Journal International*, 236(1):659–674, Nov. 2023. doi: 10.1093/gji/ggad449.
- Chen, X. Source parameter analysis using distributed acoustic sensing – an example with the PoroTomo array. *Geophysical Journal International*, 233(3):2208–2214, Feb. 2023. doi: 10.1093/gji/ggad061.
- Chen, Y., Savvaidis, A., Fomel, S., Chen, Y., Saad, O. M., Wang, H., Oboué, Y. A. S. I., Yang, L., and Chen, W. Denoising of Distributed Acoustic Sensing Seismic Data Using an Integrated Framework. *Seismological Research Letters*, 94(1):457–472, Nov. 2022. doi: 10.1785/0220220117.
- De Siena, L., Thomas, C., and Aster, R. Multi-scale reasonable attenuation tomography analysis (MuRAT): An imaging algorithm designed for volcanic regions. *Journal of Volcanology and Geothermal Research*, 277:22–35, May 2014. doi: 10.1016/j.jvolgeores.2014.03.009.
- Delsanto, P. P. *Universality of nonclassical nonlinearity*. Springer, Torino, 2006.
- Du, Z., Foulger, G. R., and Mao, W. Noise reduction for broad-band, three-component seismograms using data-adaptive polarization filters. *Geophysical Journal International*, 141(3):820–828, June 2000. doi: 10.1046/j.1365-246x.2000.00156.x.
- Edwards, B., Kraft, T., Cauzzi, C., Kastli, P., and Wiemer, S. Seismic monitoring and analysis of deep geothermal projects in St Gallen and Basel, Switzerland. *Geophysical Journal International*, 201(2):1022–1039, Mar. 2015. doi: 10.1093/gji/ggv059.
- Feigl, K., Reinisch, E., Patterson, J., Jreij, S., Parker, L., Nayak, A., Zeng, X., Cardiff, M., Lord, N. E., Fratta, D., Thurber, C., Wang, H., Robertson, M., Coleman, T., Miller, D. E., Spielman, P., Akerley, J., Kreemer, C., Morency, C., Matzel, E., Trainor-Guitton, W., and Davatzes, N. PoroTomo Natural Laboratory Horizontal and Vertical Distributed Acoustic Sensing Data, 2016. doi: 10.15121/1778858.
- Fernandez-Ruiz, M. R., Martins, H. F., Williams, E. F., Becerril, C., Magalhaes, R., Costa, L., Martin-Lopez, S., Jia, Z., Zhan, Z., and Gonzalez-Herraez, M. Seismic Monitoring With Distributed Acoustic Sensing From the Near-Surface to the Deep Oceans. *Journal of Lightwave Technology*, 40(5):1453–1463, Mar. 2022. doi: 10.1109/jlt.2021.3128138.
- Grandi, S., Dean, M., and Tucker, O. Efficient Containment Monitoring with Distributed Acoustic Sensing: Feasibility Studies for the Former Peterhead CCS Project. *Energy Procedia*, 114: 3889–3904, July 2017. doi: 10.1016/j.egypro.2017.03.1521.
- Grigoli, F., Cesca, S., Priolo, E., Rinaldi, A. P., Clinton, J. F., Stabile, T. A., Dost, B., Fernandez, M. G., Wiemer, S., and Dahm, T. Current challenges in monitoring, discrimination, and management of induced seismicity related to underground industrial activities: A European perspective. *Reviews of Geophysics*, 55(2):310–340, Apr. 2017. doi: 10.1002/2016rg000542.
- Hanks, T. C. and Kanamori, H. A moment magnitude scale. *Journal of Geophysical Research: Solid Earth*, 84(B5):2348–2350, May 1979. doi: 10.1029/jb084ib05p02348.
- Harmon, N., Rychert, C. A., Davis, J., Brambilla, G., Buffet, W., Chichester, B., Dai, Y., Bogiatzis, P., Snook, J., van Putten, L., and Masoudi, A. Surface deployment of DAS systems: Coupling strategies and comparisons to geophone data. *Near Surface Geophysics*, 20(5):465–477, Aug. 2022. doi: 10.1002/nsg.12232.
- Hubbard, P. G., Vantassel, J. P., Cox, B. R., Rector, J. W., Yust, M. B. S., and Soga, K. Quantifying the Surface Strain Field Induced by Active Sources with Distributed Acoustic Sensing: Theory and Practice. *Sensors*, 22(12):4589, June 2022. doi: 10.3390/s22124589.
- Hudson, T. Data associated with the study: Unlocking DAS amplitude information through coherency coupling quantification, 2024. doi: 10.5281/ZENODO.13684046.
- Hudson, T. S., Baird, A. F., Kendall, J. M., Kufner, S. K., Brisbourne, A. M., Smith, A. M., Butcher, A., Chalari, A., and Clarke, A. Distributed Acoustic Sensing (DAS) for Natural Microseismicity Studies: A Case Study From Antarctica. *Journal of Geophysical Research: Solid Earth*, 126(7), July 2021. doi: 10.1029/2020jb021493.
- Hudson, T. S., Asplet, J., and Walker, A. M. Automated shear-wave splitting analysis for single- and multi-layer anisotropic media. *Seismica*, 2(2), Oct. 2023a. doi: 10.26443/seismica.v2i2.1031.
- Hudson, T. S., Kendall, J. M., Blundy, J. D., Pritchard, M. E., MacQueen, P., Wei, S. S., Gottsmann, J. H., and Lapins, S. Hydrothermal Fluids and Where to Find Them: Using Seismic Attenuation and Anisotropy to Map Fluids Beneath Uturuncu Volcano, Bolivia. *Geophysical Research Letters*, 50(5), Feb. 2023b. doi: 10.1029/2022gl100974.
- Hudson, T. S., Klaasen, S., Fontaine, O., Bacon, C. A., Jónsdóttir, K., and Fichtner, A. Towards a widely applicable earthquake detection algorithm for fibreoptic and hybrid fibreoptic-seismometer networks. *Geophysical Journal International*, 240(3):1965–1985, Jan. 2025. doi: 10.1093/gji/ggae459.
- Igel, J. K. H., Klaasen, S., Noe, S., Nomikou, P., Karantzalos, K., and Fichtner, A. Challenges in submarine fiber-optic earthquake monitoring. May 2024. doi: 10.22541/es-soar.171691177.74747140/v1.
- Jousset, P., Currenti, G., Schwarz, B., Chalari, A., Tilmann, F., Reinsch, T., Zuccarello, L., Privitera, E., and Krawczyk, C. M. Fibre optic distributed acoustic sensing of volcanic events. *Nature Communications*, 13(1), Mar. 2022. doi: 10.1038/s41467-022-29184-w.
- Klaasen, S., Paitz, P., Lindner, N., Dettmer, J., and Fichtner, A. Distributed Acoustic Sensing in Volcano-Glacial Environments—Mount Meager, British Columbia. *Journal of Geophysical Research: Solid Earth*, 126(11), Nov. 2021. doi: 10.1029/2021jb022358.
- Kufner, S., Wookey, J., Brisbourne, A. M., Martín, C., Hudson, T. S., Kendall, J. M., and Smith, A. M. Strongly Depth-Dependent Ice Fabric in a Fast-Flowing Antarctic Ice Stream Revealed With Icequake Observations. *Journal of Geophysical Research: Earth Surface*, 128(3), Mar. 2023. doi: 10.1029/2022jf006853.

- Lapins, S., Butcher, A., Kendall, J.-M., Hudson, T. S., Stork, A. L., Werner, M. J., Gunning, J., and Brisbourne, A. M. DAS-N2N: machine learning distributed acoustic sensing (DAS) signal denoising without clean data. *Geophysical Journal International*, 236(2):1026–1041, Nov. 2023. doi: 10.1093/gji/ggad460.
- Lawrence, J. F. and Prieto, G. A. Attenuation tomography of the western United States from ambient seismic noise. *Journal of Geophysical Research*, 116(B6), June 2011. doi: 10.1029/2010jb007836.
- Lecoulant, J., Ma, Y., Dettmer, J., and Eaton, D. Strain-based forward modeling and inversion of seismic moment tensors using distributed acoustic sensing (DAS) observations. *Frontiers in Earth Science*, 11, June 2023. doi: 10.3389/feart.2023.1176921.
- Lellouch, A. and Biondi, B. L. Seismic Applications of Downhole DAS. *Sensors*, 21(9):2897, Apr. 2021. doi: 10.3390/s21092897.
- Lellouch, A., Lindsey, N. J., Ellsworth, W. L., and Biondi, B. L. Comparison between Distributed Acoustic Sensing and Geophones: Downhole Microseismic Monitoring of the FORGE Geothermal Experiment. *Seismological Research Letters*, 91(6):3256–3268, Aug. 2020. doi: 10.1785/0220200149.
- Lellouch, A., Schultz, R., Lindsey, N., Biondi, B., and Ellsworth, W. Low-Magnitude Seismicity With a Downhole Distributed Acoustic Sensing Array—Examples From the FORGE Geothermal Experiment. *Journal of Geophysical Research: Solid Earth*, 126(1), 2021. doi: 10.1029/2020jb020462.
- Li, J., Zhu, W., Biondi, E., and Zhan, Z. Earthquake focal mechanisms with distributed acoustic sensing. *Nature Communications*, 14(1), July 2023. doi: 10.1038/s41467-023-39639-3.
- Lindsey, N. J. and Martin, E. R. Fiber-Optic Seismology. *Annual Review of Earth and Planetary Sciences*, 49(1):309–336, May 2021. doi: 10.1146/annurev-earth-072420-065213.
- Lindsey, N. J., Rademacher, H., and Ajo-Franklin, J. B. On the Broadband Instrument Response of Fiber-Optic DAS Arrays. *Journal of Geophysical Research: Solid Earth*, 125(2), Feb. 2020. doi: 10.1029/2019jb018145.
- Lior, I., Rivet, D., Ampuero, J.-P., Sladen, A., Barrientos, S., Sánchez-Olavarría, R., Villarroel Opazo, G. A., and Bustamante Prado, J. A. Magnitude estimation and ground motion prediction to harness fiber optic distributed acoustic sensing for earthquake early warning. *Scientific Reports*, 13(1), Jan. 2023. doi: 10.1038/s41598-023-27444-3.
- Liu, X., Beroza, G. C., Yang, L., and Ellsworth, W. L. Ambient noise Love wave attenuation tomography for the LASSIE array across the Los Angeles basin. *Science Advances*, 7(22), May 2021. doi: 10.1126/sciadv.abe1030.
- Martin, E. R. Passive imaging and characterization of the subsurface with DAS. *PhD thesis*, 2018.
- Martin, T. and Nash, G. Utah FORGE: High-Resolution DAS Microseismic Data from Well 78-32, 2019. doi: 10.15121/1603679.
- Muir, J. B. and Zhan, Z. Wavefield-based evaluation of DAS instrument response and array design. *Geophysical Journal International*, 229(1):21–34, Oct. 2021. doi: 10.1093/gji/ggab439.
- Naderyan, V., Hickey, C. J., and Raspet, R. Wind-induced ground motion. *Journal of Geophysical Research: Solid Earth*, 121(2): 917–930, Feb. 2016. doi: 10.1002/2015jb012478.
- Nakata, N., Chang, J. P., Lawrence, J. F., and Boué, P. Body wave extraction and tomography at Long Beach, California, with ambient-noise interferometry. *Journal of Geophysical Research: Solid Earth*, 120(2):1159–1173, Feb. 2015. doi: 10.1002/2015jb011870.
- Ostrander, W. J. Plane-wave reflection coefficients for gas sands at nonnormal angles of incidence. *GEOPHYSICS*, 49(10): 1637–1648, Oct. 1984. doi: 10.1190/1.1441571.
- Ostrovsky, L. A. Wave processes in media with strong acoustic non-linearity. *The Journal of the Acoustical Society of America*, 90(6): 3332–3337, Dec. 1991. doi: 10.1121/1.401444.
- Paitz, P., Edme, P., Gräff, D., Walter, F., Doetsch, J., Chalari, A., Schmelzbach, C., and Fichtner, A. Empirical Investigations of the Instrument Response for Distributed Acoustic Sensing (DAS) across 17 Octaves. *Bulletin of the Seismological Society of America*, 111(1):1–10, Oct. 2020. doi: 10.1785/0120200185.
- Prieto, G., Parker, R., and Vernon III, F. A Fortran 90 library for multitaper spectrum analysis. *Computers & Geosciences*, 35(8): 1701–1710, Aug. 2009a. doi: 10.1016/j.cageo.2008.06.007.
- Prieto, G. A., Lawrence, J. F., and Beroza, G. C. Anelastic Earth structure from the coherency of the ambient seismic field. *Journal of Geophysical Research: Solid Earth*, 114(B7), July 2009b. doi: 10.1029/2008jb006067.
- Reinsch, T., Thurley, T., and Jousset, P. On the mechanical coupling of a fiber optic cable used for distributed acoustic/vibration sensing applications - A theoretical consideration. *Measurement Science and Technology*, 28(12):127003, Nov. 2017. doi: 10.1088/1361-6501/aa8ba4.
- Reiss, M. C., De Siena, L., and Muirhead, J. D. The Interconnected Magmatic Plumbing System of the Natron Rift. *Geophysical Research Letters*, 49(15), Aug. 2022. doi: 10.1029/2022gl098922.
- Samson, J. C. and Olson, J. V. Data-adaptive polarization filters for multichannel geophysical data. *GEOPHYSICS*, 46(10): 1423–1431, Oct. 1981. doi: 10.1190/1.1441149.
- Shearer, P. M. and Orcutt, J. A. Surface and near-surface effects on seismic waves—theory and borehole seismometer results. *Bulletin of the Seismological Society of America*, 77(4):1168–1196, Aug. 1987. doi: 10.1785/bssa0770041168.
- Sladen, A., Rivet, D., Ampuero, J. P., De Barros, L., Hello, Y., Calbris, G., and Lamare, P. Distributed sensing of earthquakes and ocean-solid Earth interactions on seafloor telecom cables. *Nature Communications*, 10(1), Dec. 2019. doi: 10.1038/s41467-019-13793-z.
- Spica, Z. J., Castellanos, J. C., Viens, L., Nishida, K., Akuhara, T., Shinohara, M., and Yamada, T. Subsurface Imaging With Ocean-Bottom Distributed Acoustic Sensing and Water Phases Reverberations. *Geophysical Research Letters*, 49(2), Jan. 2022. doi: 10.1029/2021gl095287.
- Stork, A., Verdon, J., and Kendall, J. The robustness of seismic moment and magnitudes estimated using spectral analysis. *Geophysical Prospecting*, 62(4):862–878, May 2014. doi: 10.1111/1365-2478.12134.
- Trabattoni, A., Biagioli, F., Strumia, C., van den Ende, M., Scotto di Uccio, F., Festa, G., Rivet, D., Sladen, A., Ampuero, J. P., Métaixian, J.-P., and Stutzmann, M. From strain to displacement: using deformation to enhance distributed acoustic sensing applications. *Geophysical Journal International*, 235(3):2372–2384, Sept. 2023. doi: 10.1093/gji/ggad365.
- van den Ende, M., Lior, I., Ampuero, J.-P., Sladen, A., Ferrari, A., and Richard, C. A Self-Supervised Deep Learning Approach for Blind Denoising and Waveform Coherence Enhancement in Distributed Acoustic Sensing Data. *IEEE Transactions on Neural Networks and Learning Systems*, 34(7):3371–3384, July 2023. doi: 10.1109/tnnls.2021.3132832.
- Viens, L. and Delbridge, B. G. Shallow Soil Response to a Buried Chemical Explosion With Geophones and Distributed Acoustic Sensing. *Journal of Geophysical Research: Solid Earth*, 129(7), July 2024. doi: 10.1029/2023jb028416.
- Walter, F., Gräff, D., Lindner, F., Paitz, P., Köpfl, M., Chmiel, M., and Fichtner, A. *Distributed Acoustic Sensing of Microseismic Sources and Wave Propagation in Glaciated Terrain*, page 1–30. Cambridge University Press, Mar. 2014. doi:

10.1017/cbo9781107415324.004.

Wang, H. F., Zeng, X., Miller, D. E., Fratta, D., Feigl, K. L., Thurber, C. H., and Mellors, R. J. Ground motion response to an ML 4.3 earthquake using co-located distributed acoustic sensing and seismometer arrays. *Geophysical Journal International*, 213(3): 2020–2036, Mar. 2018. doi: 10.1093/gji/ggy102.

Williams, E. F., Zhan, Z., Martins, H. F., Fernández-Ruiz, M. R., Martín-López, S., González-Herráez, M., and Callies, J. Surface Gravity Wave Interferometry and Ocean Current Monitoring With Ocean-Bottom DAS. *Journal of Geophysical Research: Oceans*, 127(5), May 2022. doi: 10.1029/2021jc018375.

Wuestefeld, A., Stokkan, S., Baird, A., and Oye, V. NOR-FROST: A near-surface test site for fibre optic sensing. In *EAGE GeoTech 2021 Second EAGE Workshop on Distributed Fibre Optic Sensing*. European Association of Geoscientists Engineers, 2021. doi: 10.3997/2214-4609.202131027.

Yang, L., Fomel, S., Wang, S., Chen, X., and Chen, Y. Denoising distributed acoustic sensing data using unsupervised deep learning. *GEOPHYSICS*, 88(4):V317–V332, July 2023. doi: 10.1190/geo2022-0460.1.

Yang, X., Bryan, J., Okubo, K., Jiang, C., Clements, T., and Denolle, M. A. Optimal stacking of noise cross-correlation functions. *Geophysical Journal International*, 232(3):1600–1618, Oct. 2022. doi: 10.1093/gji/ggac410.

Yin, J., Zhu, W., Li, J., Biondi, E., Miao, Y., Spica, Z. J., Viens, L., Shinohara, M., Ide, S., Mochizuki, K., Husker, A. L., and Zhan, Z. Earthquake Magnitude With DAS: A Transferable Data-Based Scaling Relation. *Geophysical Research Letters*, 50(10), May 2023. doi: 10.1029/2023gl103045.

Zhan, Z. Distributed Acoustic Sensing Turns Fiber-Optic Cables into Sensitive Seismic Antennas. *Seismological Research Letters*, 91(1):1–15, Dec. 2019. doi: 10.1785/0220190112.

The article *Unlocking distributed acoustic sensing amplitude information through coherency coupling quantification* © 2025 by Thomas S. Hudson is licensed under CC BY 4.0.